2014 NDIA GROUND VEHICLE SYSTEMS ENGINEERING AND TECHNOLOGY SYMPOSIUM
MODELING & SIMULATION, TESTING AND VALIDATION (MSTV) TECHNICAL SESSION
AUGUST 12-14, 2014 – NOVI, MICHIGAN

MULTI-RESOLUTION RAPID PROTOTYPING OF VEHICLE COOLING SYSTEMS: Approach and Test Results

Maciej Z. Pindera, PhD,	Jean-Jacques Malosse, PhD,	Yuzhi Sun, PhD,	Steven R. Vosen, PhD
Computational Sciences, LLC, Madison, AL			
Mary Goryca			
U.S. Army RDECOM-TARDEC			

ABSTRACT

This paper describes multi-resolution, distributed design and simulation software for rapid prototyping and analysis of complex systems using a Co-simulation approach. The current focus of this work is on the modeling of the engine cooling system in the Ford Escape Hybrid SUV vehicle. In that particular vehicle the cooling system consists of three coupled subsystems: a) engine cooling; b) electronic transaxle cooling; and battery cooling. This paper discusses two aspects of this work: a) high level description of the developed models and co-simulation approaches; and b) comparison of co-simulation to test data. Most of the model predictions deviated from the test data by less than 5%. Results indicate that distributed multi-resolution simulations can significantly accelerate the analysis of flow-thermal processes in complex vehicle systems. Moreover, the approach allows coupling of different codes with different functionalities to obtain integrated results not possible with any one individual code.

1. INTRODUCTION

Many physical systems can be of sufficient complexity (both geometric and physics-related) to make fully resolved 3D simulations impractical due to complicated gridding requirements and potentially very slow execution times on complex grids. Moreover, a single software package may not have all the capabilities required for complete vehicle thermal analysis. Modern army and commercial vehicles with hybrid power systems that contain multiple heat-generating and rejection components are one example of such systems, as shown in Figure 1. This particular system shows three independent but coupled cooling loops: engine, motor-electronics (M/E) module and the battery pack using the A/C system.

The distributed multi-resolution approach sidesteps these difficulties by: a) partitioning a complex system into interacting components that can be represented by reduced models of varying levels of fidelity; and b) using several codes in coupled parallel or parallel/series execution, each performing a set of specific computational tasks and exchanging information in real time. For generality, information exchange takes place with the aid of a simulation environment that allows inclusion of additional system component models and legacy codes with minimal code modifications. Such a computing approach is also known as *grid*, or *co-simulation*.

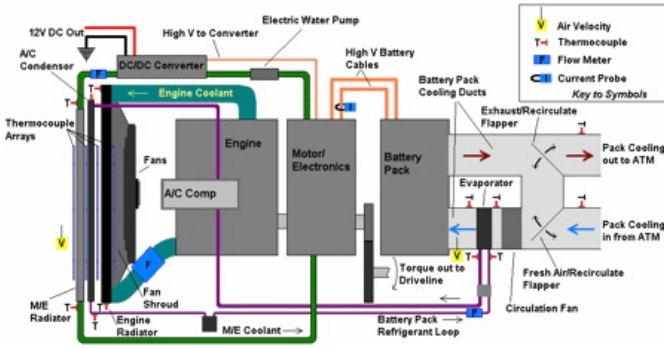

Figure 1: Multi-component Cooling System in a Ford Escape Hybrid

The examples discussed in this paper show the advantages of this approach for analysis of complex systems. The multi-resolution co-simulation methods allow the use of the time-intensive, high-fidelity models only where needed, with the rest of the system being modeled using much faster, lower resolution approaches.

2. MULTI-RESOLUTION ANALYSIS

Multi-resolution analysis partitions a complex continuous system into components where each component is represented by a separate model. In our approach we have developed a general wrapper routine that encapsulates a large class of such models as stand-alone codes, with

communication interfaces that allow the codes to exchange data with one another between suitably defined boundary and/or volume conditions. This approach allows simulation of a large class of dynamic systems to different levels of accuracy since it allows coupling of models defined on 0D-3D domains. Data exchange is brokered by Open Architecture, co-simulation environment *CoSim* that connects the system components. Figure 2 shows the connection scheme for a stand-alone A/C system.

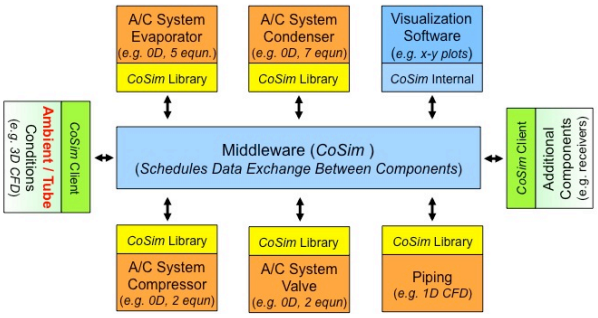

Figure 2: CoSim-Brokered A/C Connection Scheme

The component models are connected to a 3D CFD model that calculates the under-hood ambient conditions that regulate heat exchange between the system and the environment. As indicated, *CoSim* also allows visualization of a component response history during run time. The main advantage of connecting the system components through an independent environment rather than connecting them directly is that additional components can be added to the system without affecting the original connectivity or data transfer synchronization.

Although system partitioning is by necessity problem specific, the possibility of using separate codes to simulate the dynamics of different components gives this form of multi-resolution approach a large degree of latitude in how the systems are partitioned. Multi-resolution analysis can be carried out on different levels and with different requirements that may be, for example:

1. *Fully-resolved*: full 3D analysis performed on the vehicle-package system using standard CFD.
2. *Mixed-resolution*: combination of full 2D or 3D detailed/meshed model and reduced-order representations of components within the system.
3. *System-level*: assembly of reduced-order models of components for rapid generation of results for the entire vehicle-package system.
4. *Interface with legacy codes*: each code performs a different analysis task. For example, one code can generate vehicle surface heat flux data (due to internal heating) that another code will use to compute vehicle surface cooling and thermal signature.
5. *Selective focusing*: using reduced-order models (with increased resolution) on specific components/ assemblies, while using regular reduced-order models for the remaining components. This feature allows fast analyses of parametric changes in the 'focused' portions, and is extremely useful for rapid thermal prototyping, signature management, and optimization.

2.1 Simulation Environment and Data Exchange

The basic function of the simulation environment is to schedule data transfer between the different codes that comprise the system of interest. The codes do not communicate directly, but only through the environment. The environment also contains transformer functions that can be used for data scaling, rescaling, and modeling of components, and contains a user-expandable library of component models of different fidelities, common to vehicle cooling systems. The environment structure allows an arbitrary number of codes to be connected in an arbitrary fashion, and exchange an arbitrary amount and type of data. Data exchange is executed using the CORBA communications protocol [e.g. Siegel, 2007] allowing platform-to-platform data exchange over a computer network. The protocols are encapsulated in a set of Application Programming Interfaces (APIs). APIs are codelets designed to be appended to any stand-alone component code, with minimum modification to the host codes. Corresponding APIs exist in *CoSim*. Figure 3 shows a schematic of the data exchange process.

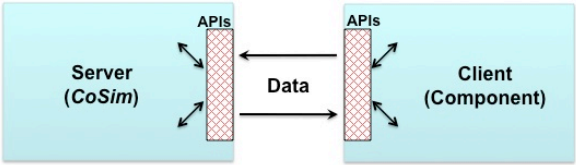

Figure 3: Server-Client connectivity Between the CoSim Environment and System Component Models

The environment executes the following functions:

1. Data reception and reception scheduling (using APIs);
2. Data distribution and sequencing to proper models;
3. Data pre-processing (mainly appropriate scaling operations);
4. Data processing (if library models are used in simulations);
5. Data post-processing (appropriate output rescaling);
6. Data transmission and scheduling (using APIs).

Data is exchanged at a rate specified by the user. Any data can be exchanged (pressure, temperature, etc.) from any point in the computational domain. The user is responsible for providing the software front-ends that will extract (impose) the required data from (to) the code of

interest and supply the data to the APIs for transmission (or reception). When component models use implicit solvers, information is typically passed every several iterations to make the simulation tightly coupled. During the multi-component, multi-resolution simulation, the environment ensures that the executions of each code and data exchange are properly synchronized. The actual data exchange process is illustrated in Figure 4 for the coupling of an example radiator model and the environment in which it is embedded.

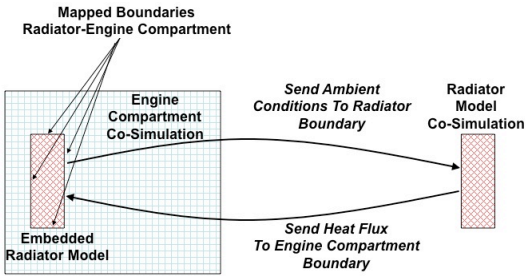

Figure 4: Data Exchange Between Reduced Models and the CFD Domain

This approach is used for communications of *any* reduced model with the associated CFD domain. A placeholder domain is defined in the CFD grid with which the reduced model is exchanging information: the CFD domain sends the ambient conditions data to the reduced model that in turn uses this (and other) information to calculate the (e.g.) heat flux that is sent back to the CFD solver.

2.2 Application to Cooling of Ford Escape SubSystems

Figure 1 shows the three major sources of heat, each of which with its own cooling loop: gasoline engine, M/E unit, and the battery pack. It was possible to accurately measure heat rejection by the various components in the cooling systems in each separate loop, using similar procedures. For each loop, working fluid (coolant or refrigerant) mass flow and temperature change across each component was measured using turbine flow meters and thermocouples, respectively. Air velocities through the heat exchangers were measured directly and mass flow rates were estimated from temperature measurements using arrays of thermocouples. Radiator fan speeds were measured optically. The following general types of measurements were performed.

Engine Cooling: was modeled by connecting the following components together: engine; pump; radiator, piping, as well as engineEnvironment (for setting load/speed parameters) and radiatorEnvironment (for specifying data exchange with the CFD underHood model). The measurements included: *coolant mass flow, temperature measurements across the engine, temperature and air mass flow across the radiator.*

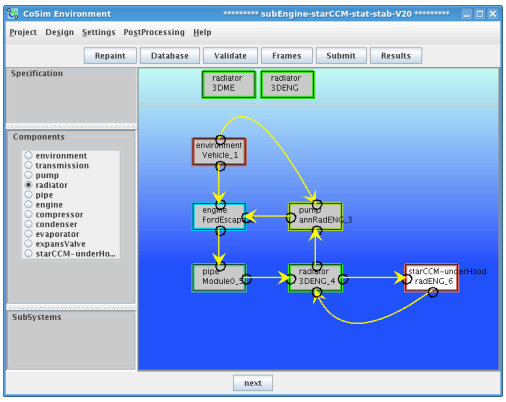

Figure 5: Modeling the Engine Cooling Loop

Figure 5 shows the configuration of this system, along with the information flow. We have performed a number of system-level demonstration simulations that show the component and system response. Figure 6 shows an example of transient response to a perturbation to vehicle speed.

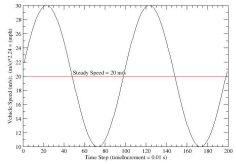

a) Variation in vehicle speed

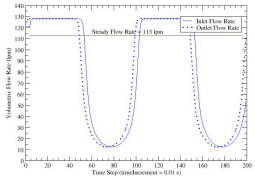

b) Resultant coolant flow in pump

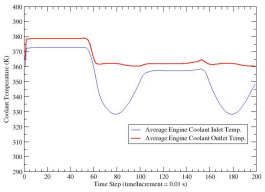

c) Temp. increase across engine

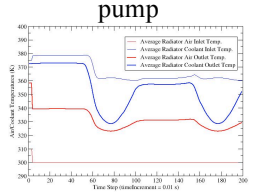

d) Temperature changes in radiator

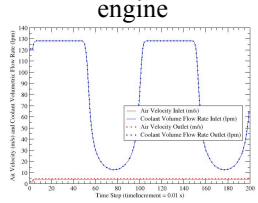

e) Flow rates in radiator

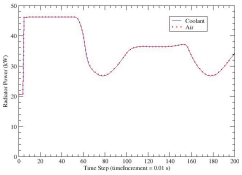

f) Measures of radiator power

***Figure 6*:** Ford Engine Cooling Loop Response to 50% Speed Perturbation

It can be seen that all calculations are stable, and the pump is operating near its upper limit: increases in the vehicle speed have little effect on the resultant pumping

rate. The opposite (not shown) is true as the vehicle speed decreases: coolant flow rate decreases notably, as expected.

M/E Unit Cooling: We have again connected six components that form the transaxle cooling subSystem. The cooling configuration is shown in Figure 7.

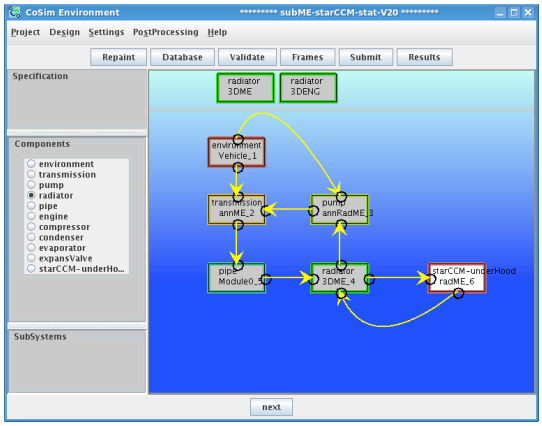

Figure 7: Modeling the M/E Unit Cooling Loop

The components and the information flow are similar to that for the engine, replacing the latter with transaxle model, the engine pump with transaxle pump, and the engine radiator configuration with one appropriate for transaxle cooling. The measurements were the same as for the engine: *coolant mass flow, temperature measurements across the transaxle, temperature and air mass flow across the radiator.* This system is also *strongly coupled* since changes in the radiator outlet coolant temperatures directly affect the temperature increase across the transmission.

As for the engine, we have performed a number of system-level demonstration simulations that show the component and system response. Figure 8 shows an example of transient response to a perturbation to vehicle speed. We see the same mass flow trends that we have observed for load variation: noticeable coolant flow increase with increasing vehicle velocity, and smaller flow increase with decreasing velocity. Again, calculations are stable. Note the slight increase in exit air velocity due to air heat-up, as shown in panel (e). We note that although the radiator dimensions for the transaxle and engine radiators are similar, ICE engine coolant flow rate is more than an order of magnitude higher than in the transaxle cooling subSystem, since the former generates considerably more heat than the latter. This increased heat results in considerably higher temperatures and radiator powers, than for the transaxle. System responses to variations in the vehicle speed conditions are also much less pronounced.

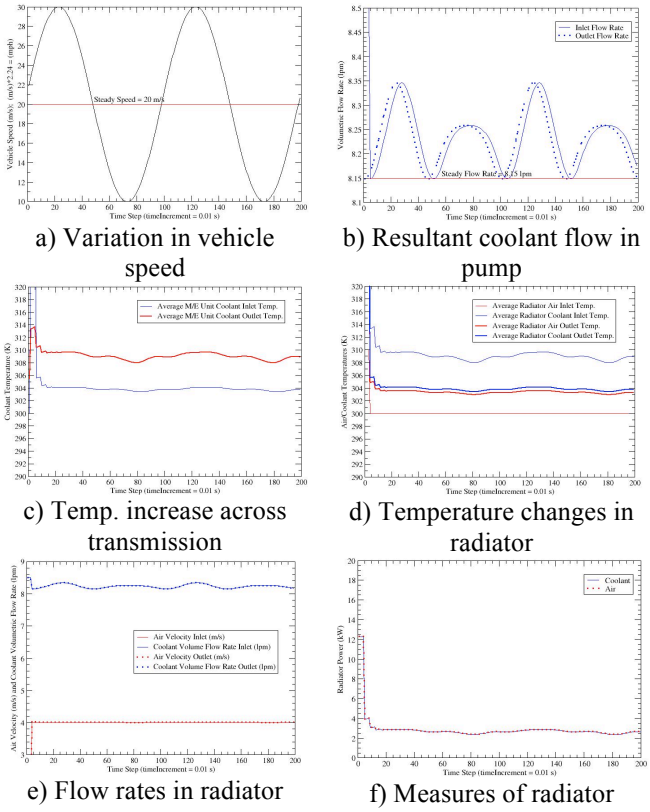

a) Variation in vehicle speed

b) Resultant coolant flow in pump

c) Temp. increase across transmission

d) Temperature changes in radiator

e) Flow rates in radiator

f) Measures of radiator power

***Figure 8*:** Ford Transmission Cooling Loop Response to 50% Speed Perturbation

Battery Pack Cooling: Figure 9 shows the configuration of this system, along with information flow.

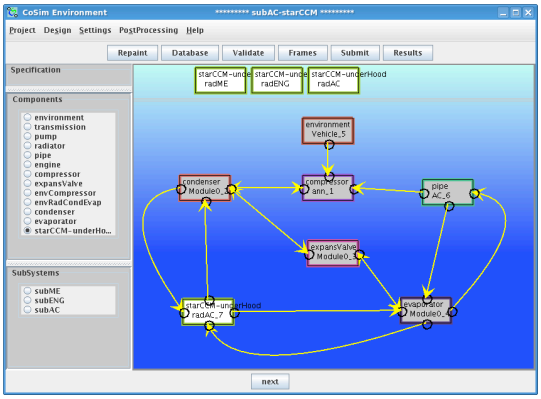

Figure 9: Modeling the A/C Cooling Loop
(7 Interconnected Elements; strongly coupled)

The system was modeled by connecting the following components together: condenser, evaporator, compressor, expansion valve, piping, as well as the vehicleEnvironment (for setting A/C operating parameters) and evaporator

CondenserEnvironment (for specifying data exchange with the CFD underHood model).

As for the engine and the transaxle, we have performed a number of system-level demonstration simulations that show the component and system response. Figure 10 shows an example of transient evaporator pressure and temperature responses to perturbations in the refrigerant flow rates. Once again, all the calculations are stable.

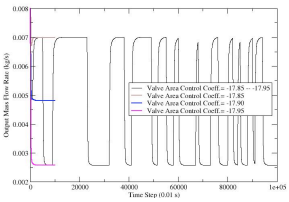

a) Compressor mass flow rate

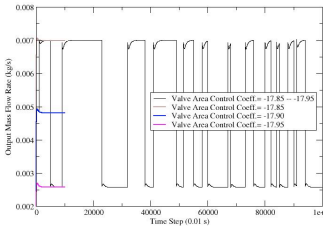

b) Expansion valve mass flow rate

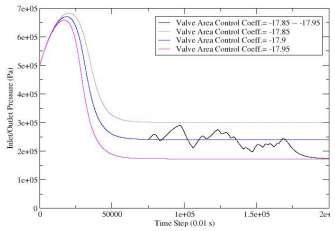

c) Pressure response for long tube evaporator

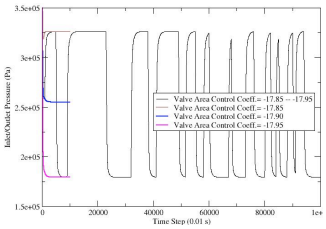

d) Pressure response for short tube evaporator

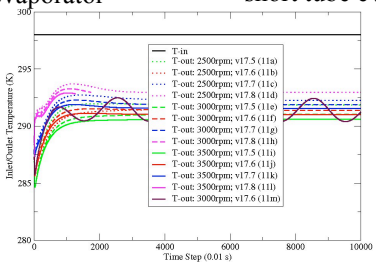

e) Evaporator temperature response to flowrate variations

Figure 10: Component Responses to Variations in Valve Area Control Parameter u for the Ford Escape A/C System

2.3 Application to Cooling of Ford Escape System

The complete cooling system consists of the three subSystems discussed previously. To demonstrate stable interactions with a more realistic environment, we have connected the four heat exchangers (two radiators, condenser and the evaporator) to the STAR-CCM+ CFD code that simulates the 3D thermal-flow fields in very simplified underHood (for heat rejection) and battery compartment (for heat absorption) domains. Figure 11 shows the complete system as represented by the interconnected subSystems. We note that the following results are qualitative in nature since the simulations were performed using a very simplified computational domain.

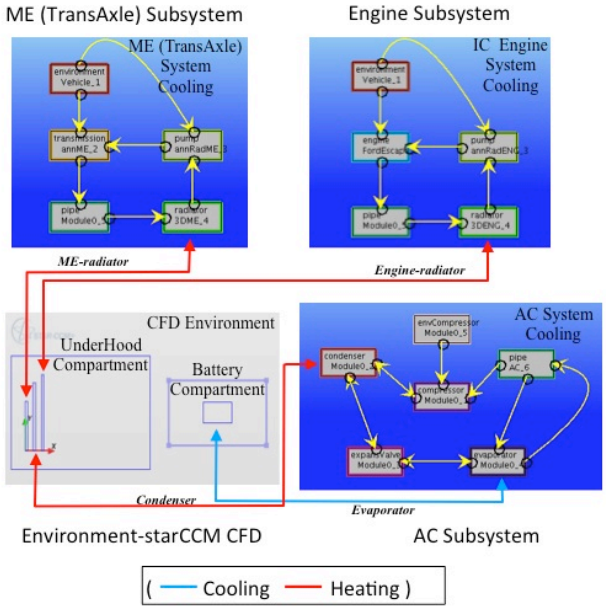

Figure 11: Schematic of the complete system

The CFD domain was divided into two isolated subDomains, underHood and the battery compartment, each using different sources of external air. The two do however communicate indirectly through the refrigerant in the A/C system that heats up through battery cooling, and cools down through heat rejection in the underHood domain. Two mesh models and two physical models were selected for those two domains, respectively. Unstructured hexahedron grids were generated using the 3D-CAD facility in starCCM+.

Figure 12a shows the composite environment indicating the embedded heat exchangers and the respective air flows. In this co-simulation, starCCM+ provided the air velocity, temperature and pressure to the four heat exchangers. The direction of the air velocity vectors determined the direction of data exchange: the front face was in the upwind direction and the rear face was downwind. CFD data on the front face of the heat exchangers was mapped onto the local exchanger face boundary, and was then passed to the exchanger models. The models then calculated a new thermal state of the exiting air at the rear face, which was then mapped onto the corresponding position in the CFD domain. The grid mapping procedures were used on the 8 interacting faces (4 components times 2 faces/component) that connected the CFD and the heat exchanger model domains.

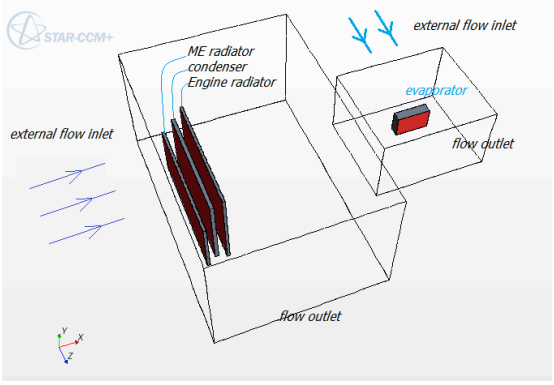

a) Overall geometry amd boundary conditions

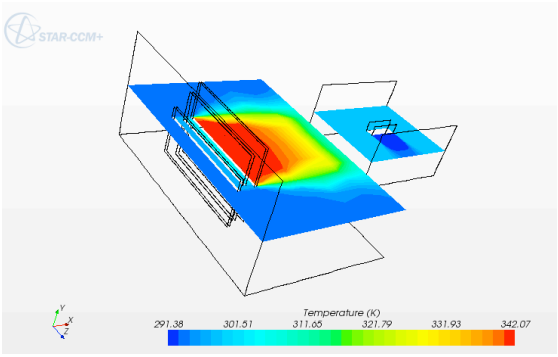

b) Air temperatures: underHood and battery domains

Figure 12: Geometry and boundary condition of a vehicle cooling system

Unsteady simulations were performed in which data exchange between the system components was executed at every time step, with 100 iterations per time step. Figure 12b shows temperature distributions at a selected timestamp, in the two compartments in the middle cutting-plane. The case was based on the operations of the Ford Escape test vehicle, using the Escape's component geometries with the following compressor and valve coefficients: compressor speed = 3000 RPM; valve area control parameter u = 17.6. We note that the underHood and the battery compartments are grossly simplified since the intent of the simulations is not to predict the cooling characteristics of this particular test vehicle, but to show the capabilities for mixed-resolution simulations of *any* vehicle (or other) cooling systems. It can be seen that the underHood heat exchangers (transaxle radiator, condenser and ICE engine radiator) heat the environment, whereas the battery heat exchanger (evaporator) cools the battery domain. The results are as expected and are physically reasonable. For this configuration, there is little difference between steady and unsteady simulations.

3. DATA COMPARISON

This section documents the performance of the reduced models with comparisons to vehicle test data. The data were generated from 35 measurements made at 7 different speeds (10 mph, 20 mph, 30 mph, 40 mph, 50 mph, 60 mph and 70 mph) and 5 different vehicle loads. Each run lasted 60 seconds (except for 30 seconds at wide open throttle) and a measurement was made every second. For each measurement, 120 different physical quantities were acquired. Therefore $7 \times 5 \times 120 \times 60 = 252{,}000$ raw data points were recorded.

3.1 Test Uncertainties and Data Post-Processing

As will be seen in the following, considerable post-processing was required in order to make meaningful comparisons between the models and experiments. In some cases data scatter was significantly high, greater than the average values of the measured quantities. In other cases, comparison data had to be inferred. For this inferred data, the following two variables associated with the A/C system were of main concern.

3.1.1 Temperature: *evaporator*— These data were taken only across the expansion valve, but not at the evaporator outlet. This quantity was inferred from other measurements as follows. We estimated the inlet enthalpy from the inlet valve temperature, estimating the pressure and noting that: a) the liquid enthalpy varies very little with pressure, and b) flow across the valve is essentially isenthalpic. The quality was estimated from the inlet temperature and enthalpy, using the lever rule for enthalpy in the two-phase region (that is $h_{tot} = xh_l + (1-x)h_g$; x = fluid quality). We assumed that the inlet enthalpy to the evaporator is equal to the outlet enthalpy to the valve. The evaporator outlet temperature was estimated by noting that the valves are typically tuned so that the temperature difference across evaporators is in the range 5-10 ^{o}C. Furthermore, the bulk of the enthalpy received by the evaporator occurs in the two-phase region and thus the enthalpy received in the gaseous region is small compared to the former. Thus, the error in estimating the evaporator outlet enthalpy remains relatively small. For all evaporator comparisons, we chose the midway point so that the refrigerant at the outlet is heated by 7 ^{o}C over the inlet. Data across the *condenser* were well defined.

3.1.2 Pressure: both the evaporator and condenser.

1 *Evaporator* pressure was estimated from the inlet refrigerant temperature, noting that pressure depends only on temperature that *does not change appreciably*.

2 *Condenser* pressure was estimated at 1.6 MPa, based on typical condenser operations. This pressure is required for specification of the inlet enthalpy of the

refrigerant that is in the gas state and varies with both temperature and pressure.

3.1.3 Data Consistency Checks— A more serious problem with experimental comparisons was related to the quality of test data, and in particular to data for the heat exchangers. Closer examination showed that the measured data was inconsistent, in the sense that radiator powers measured from airside and liquid-side (coolant) measurements did not match within a reasonable range. Here, heat exchanger power P is defined by $P_{cool/air} = \dot{m}_{cool/air} C_{p,cool/air} \delta T_{cool/air}$. Explicitly, coolant and airside powers are $P_c = \dot{m}_c C_{p,c} \delta T_c$, $P_a = \rho_a A v_a C_{p,a} \delta T_a$. The differences $(\delta T_a, \delta T_c)$ were measured at front and back faces, and coolant inlets and outlets, respectively. Under ideal conditions we expect that $P_a = P_c$. However, many measurement conditions were far from ideal and very often measurements were recorded for which $P_a \neq P_c$. Thus as an aid to data interpretation, all the comparisons for heat exchanger data include the power consistency checks.

3.1.4 Averaging of Values and Other Uncertainties— Although both the experiments and models use spatially local data, final comparisons were based on spatially averaged data for the heat exchanger airside temperatures and air velocities. Tests however show high non-uniformities in both velocity and temperature fields at inlet and outlet faces of the heat exchangers. Although such nonuniformities are very likely to affect the performance of the devices, we did not take them into account. For simplicity we used an averaging process although tests showed that some data was significantly skewed/biased. Two additional uncertainties are expected:

1 Flow Data: Under some operating conditions, refrigerant flows were in the laminar-turbulent transitions region. For such regions, heat transfer coefficients (crucial for model performance) are not very reliable.
2 Heat Exchanger Geometry: Although the overall external dimensions (e.g. core height, width, depth, number of tubes) were known, their internal structure was not. In particular the following had to be assumed: *Tube arrangement* (parallel, or serpentine), chose parallel, with 1 tube/stride; *Louvers*: chose 10 louvers/fin; inclined at 28°, height = 0.1mm; *Internal microchannels* were specified to be the same as the number of louvers; *Tube thickness*: specified 1.5 mm; *Internal wall thickness*: specified 0.3mm.

Despite the above uncertainties, model predictions were remarkably accurate in comparison to test data, and most fell within the required 5% difference.

3.2 Comparison of Generic Models

Generic models refer to formulations with no specific reference to any particular vehicle. In this case they refer to all single and multi-phase finned heat exchanger models. Details of the modeling effort are given in Pindera [2009] and Pindera et al. [2014]. The models are based on the approach proposed by Jung et al. [2006], and use an essentially gridless formulation, parameterized by the heat exchanger geometry.

The A/C system models were based on the moving boundary formulations used by Rasmussen [2002], and Shah [2003]. The system used the refrigerant R134a with the Equation of State given by Astina et al. [2004], transport properties given by Krauss et al. [1993], and thermal conductivity relations given by Yata et al. [2005].

The heat exchanger models require precise information on the tube geometry for computing the global heat transfer coefficients. However, this information is not always available and some of it was not available for the Ford Escape. To circumvent this problem, two tuning factors were introduced: one (β_A) applied to the overall geometry expressed in terms of the total participating surface area, and the other (β_h) only applied to the interior heat transfer coefficients. In general, the magnitude of these factors was in the range 1-2. A new form of the overall heat transfer coefficient accounting for the tuning factors in now written as: $U = \beta_h \left(\frac{\beta_A A_{mc}}{\eta_{mc} h_c A_{o-mc}} + \frac{t_t}{k_t} + \frac{A_t}{\eta_o h_a A_o} \right)^{-1}$, where ($A_{mc}$, A_{o-mc}, A_t, A_o) are the various surface areas associated with the heat exchanger geometry, (h_c, h_a)are the coolant and air heat transfer coefficients, (t_t, k_t) are the tube thickness and conductivity, and (η_{mc}, η_o) air-side and coolant-side fin efficiency. Experiment-model comparisons are given in terms of these factors.

3.2.1 Engine Radiator Data Consistency— The engine radiator geometry is given by: *Core Area*: 698.5 mm x 469.9 mm; *Tube Geometry:* 15.6 mm x 2.22 mm; *Tube Pitch:* 41 tubes @ 17 mm/tube. Figure 13 compares the air power P_a with the coolant power P_c for the engine radiator. We show $(P_a - P_c) / P_c$ expressed in percentages.

The measured air-based power estimates are approximately 30% higher in comparison to coolant-based estimates. One of the reasons for this discrepancy may be

due to the positioning of the air-velocity probe located between the condenser and the engine radiator. For probe locations sufficiently far from the radiator face, air velocity going through the radiator fins would be overestimated due to partial blockage of the core by the internal radiator structure (fins, tubes and louvers). This blockage would have slowed down the air going through the radiator, and caused some air to spill out the sides of the radiator. Since we did not correct the airflow readings for such blockage effects, airspeed inside the radiator is likely to be overestimated, accounting for the higher air power values.

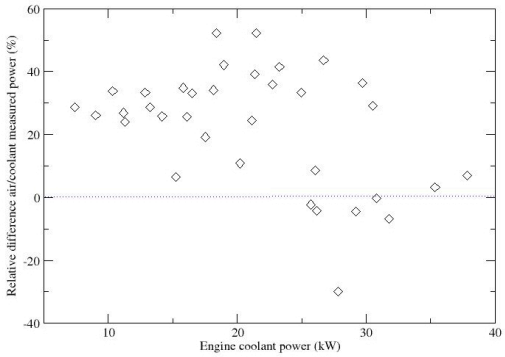

Figure 13: Relative differences between measured air and engine coolant powers

3.2.2 Engine Radiator Model Predictions— Figure 14 compares the relative differences in coolant power between model and experiments, for a 41-tube radiator. The microchannel area tuning-factor β_A was set to 1. Best fit to the experiment is obtained for tuning factor $\beta_h \simeq 1.7$.

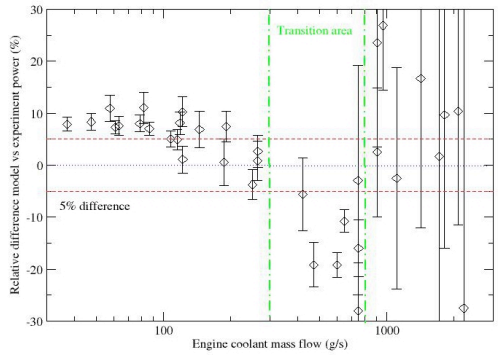

Heat transfer x 1.7

Figure 14: Comparison model/experiment data for engine coolant power for heat transfer factor=1.7

We note that in the laminar region (small mass flow rate), this difference is in the range of +10% with little scatter, while in the turbulent region, the difference is in the range of -10% with large scatter. These differences in the model prediction can be explained by the fact that we use two different heat transfer correlations for laminar and turbulent flows and by the fact that the measurements are more imprecise for high coolant mass flow (see below).

We note the following: during the measurements, air velocity has been essentially constant at approximately 1 m/s, while the coolant mass flow varied from a run to another by 2 orders of magnitude between 30 g/s and 2 kg/s. Therefore when the coolant mass flow is high, air takes out little energy per amount of coolant and therefore the difference $\delta T_c = T_2 - T_1$ is small. Measurements were taken of only T_2 and T_1 but not the temperature difference. Therefore, the relative uncertainty on the measurement of the coolant temperature difference will be large (on the order of 100% in some measurements) when the uncertainty in measured temperatures is large. This fact explains why the measured scatter on the relative difference between model and experiment is larger for high mass flows. Also for high mass flows coolant flow is turbulent while for low mass flows it is laminar. The correlations used to compute the Nusselt number Nu differ significantly in these two regimes. For laminar flow, *Nu* is a constant that only depends on the geometry of the tube (approximately 2.9) while for turbulent mass flows, the Nusselt number depends on physical, geometrical and flow parameters (see Gnielinski [1976]) Between the two flow regimes there exists an ill-defined transition zone that occurs at approximately 500 g/s. This area has been represented in green in the figures above, and it is in this area that most of the model predictions deviate from the test data.

3.2.3 Transaxle Radiator Data Consistency— The transaxle radiator geometry is given by: *Core Area*: 730.25 mm x 304.8 mm; *Tube Geometry:* 16.13 mm x 2.1 mm; *Tube Pitch:* 26 tubes @ 28 mm/tube. Figure 15 compares the air power P_a with the coolant power P_c for the engine radiator.

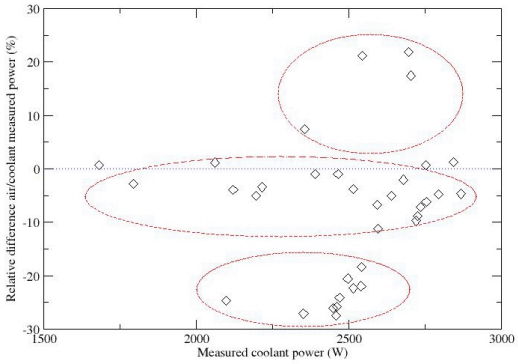

Figure 15: Relative differences between measured air and transaxle coolant powers

The figure shows that the data appears to be distributed into three groups. We do not have a clear explanation for this pattern: In the first set, air power is *underestimated* by 25%; in the second, air power is *underestimated* by only 5%; the third corresponds to the outliers mentioned below.

3.2.4 Transaxle Radiator Model Predictions— The transaxle radiator analysis (Figure 16) is similar to that performed for the engine radiator. We note that in all tests and simulations, the coolant mass flows are almost constant and are considerably smaller than those in the engine radiator: they are in the range of only 135 g/s to 150 g/s.

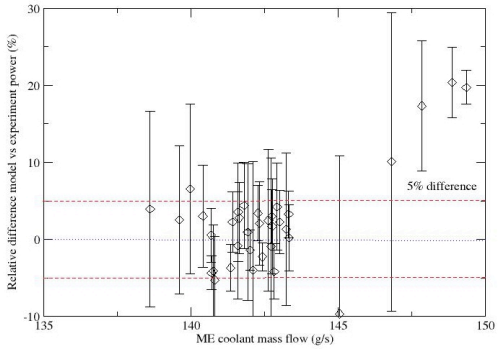

Figure 16: Comparison model/experiment data for transaxle coolant power, heat transfer factor= 2.6

These small mass flows result in laminar flow conditions for which the Nusselt number is constant at approximately 2.9. The best fit to experiment is obtained for $\beta_h = 2.6$. For both cases, most of the comparisons show that the model matches the experiment within the required 5%. Also, several model predictions at higher mass flows overestimate the power by 20% (or underestimate it by 10%). This trend seems to be associated with the outliers shown in Figure 15. It is possible that during the measurements, the coolant temperature difference may have been overestimated for these points.

3.2.5 Evaporator Data Consistency— The evaporator geometry is given by: *Core Area*: 203.2 mm x 127 mm; *Tube Geometry:* 57.15 mm x 1.7 mm; *Tube Pitch:* 10 tubes @ 12.7 mm/tube. Figure 17 compares air power P_a to refrigerant power P_r for the evaporator for full and reduced test data sets, respectively.

As discussed at the beginning of this Section 3.1, there exist problems with the integrity of data associated with A/C system operations. In the comparisons we define air-based power P_a calculations using $P_a = \rho_a A v_a C_{pa} \delta T_a$. The difference δT_a is well defined since air temperatures were measured in front and behind the evaporator. The power $P_r = \dot{m}_r (h_{out} - h_{in})$ is not well defined since refrigerant temperature has been measured *across the expansion valve*, and not across the evaporator. However, based on the discussion at the beginning of this section, these values can be estimated with a reasonable accuracy based on well-chosen assumptions. We can estimate the inlet enthalpy h_{in} and derive its saturated pressure P_{sat} from the fact that the fluid is in two-phase state. This is the refrigerant pressure inside the evaporator.

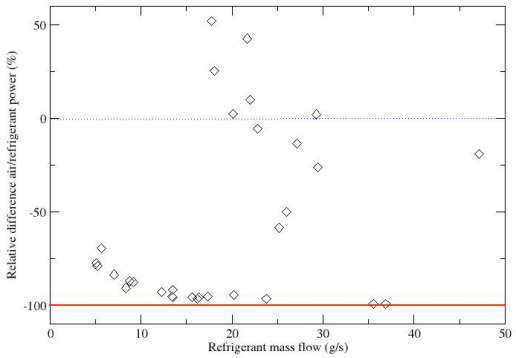

Figure 17: Comparison air/refrigerant measured powers (evaporator complete raw data)

Figure 17 shows power comparisons for all the measured 35 test points. It can be seen that for most of the data the measured air-based power estimates are considerably smaller than the estimated refrigerant-based powers that depend on the refrigerant mass flow rate. In some cases, air powers are two orders of magnitude smaller than those of the refrigerant. In such cases, the relative difference between air and refrigerant powers is close to -100%: a locus represented by a red line in the figure. This means that in practice, the evaporator is not cooling the air. The mass flow rate is derived from the volumetric flow rate by *assuming that the refrigerant is liquid.* We conclude that in these cases, the volumetric flow rate *was measured when the refrigerant was gaseous,* and therefore, the air conditioning system was not working properly.

In order to obtain data suitable for model-test comparisons, we pruned the test data by defining a cut-off ratio $P_c / P_a = 1.5$, beyond which the A/C system was deemed inoperative. This pruning reduced the number of valid test data points to 10.

Figure 18 shows the effects of this pruning on the comparison of the air power and the refrigerant power for the valid cases. Still, the remaining data is not perfect since at low mass flow rates the air power is overestimated, while at high mass flow rates the air power is underestimated. This discrepancy is likely due to the thermal inertia of the evaporator.

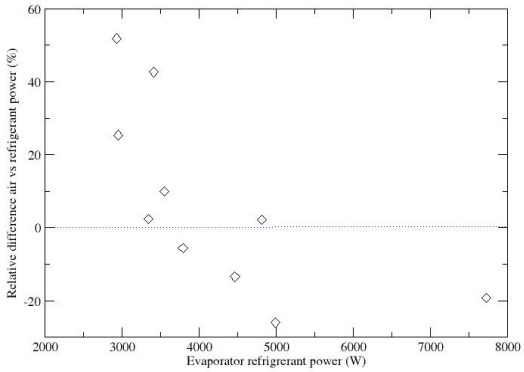

Figure 18: Comparison air/refrigerant measured powers (evaporator, pruned valid data)

3.2.6 Evaporator Model Predictions— Figure 19 compares the relative differences in coolant power between model and experiment for an evaporator.

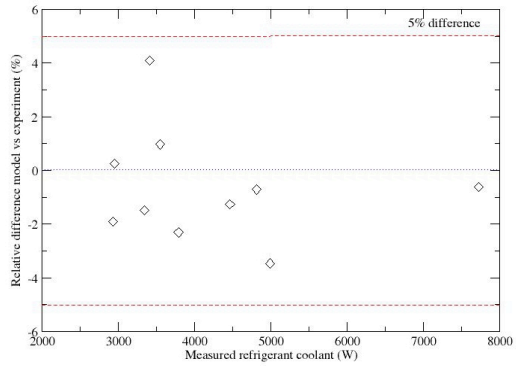

Heat transfer factor = 2

Figure 19: Comparison model/experiment for evaporator refrigerant power (fin efficiency = 0.43)

In all cases the microchannel tuning coefficient β_A was set to 1, with the insulated fin approximation, or efficiency = 0.43. Best fit to data is obtained for $\beta_H = 2$. For this value *most of the data lies within 2% and all data lies within 5%*. Such good accuracy between the model and the experiment can be explained by the fact that most of the energy transfer between the air and the refrigerant occurs when the fluid is evaporating and requires large amounts of latent heat. *In the first approximation*, the energy flux $P \approx \dot{m} \times h_{fg}$. The amount of energy transferred in the gas region is comparatively small and therefore the measurement error of the inlet and outlet temperatures will have little impact on the measured enthalpy difference.

3.2.7 Condenser Data Consistency— Condenser geometry is given by: *Core Area*: 654. mm x 419.1 mm, *Tube Geometry:* 20.32 mm x 2.18 mm; *Tube Pitch:* 41 tubes @ 10.2 mm/tube. As for the evaporator, Figure 20 compares air and P_a refrigerant power P_r for the condenser for full and reduced test data sets.

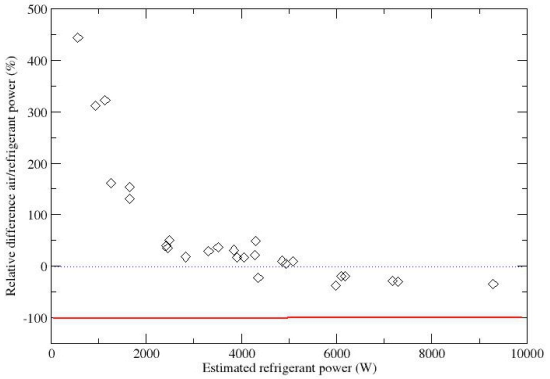

Figure 20: Comparison air/refrigerant measured powers (condenser, complete raw data)

It is seen that for the full data set (and as for the evaporator) air-based powers are overestimated for low mass flow rates. This is likely due to the fact that the body of the condenser does not cool down instantaneously and even if the A/C system stops working, the external air will still cool down the condenser.

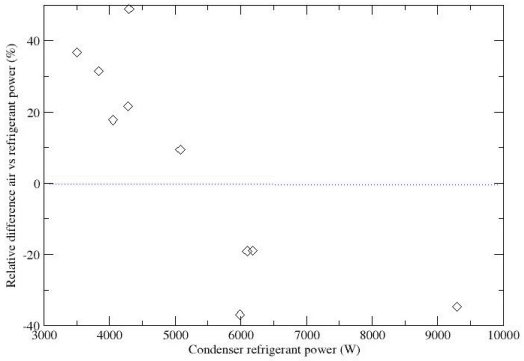

Figure 21: Comparison air/refrigerant measured powers (condenser, pruned valid data)

Figure 21 that compares the air power with the refrigerant power for the valid cases using pruned data. Again, the remaining data is not perfect since at lower mass flow rates the air power is overestimated, while at higher mass flow rates the air power is underestimated. As for the evaporator, this discrepancy is likely due to the thermal inertia of the condenser.

3.2.8 Condenser Model Prediction Comparisons— Figure 22 compares the model-test refrigerant powers for the 10 cases where the A/C was working.

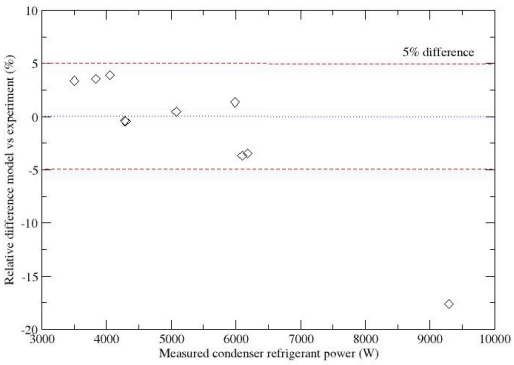

Figure 22: Comparison model/experiment for condenser refrigerant power; heat transfer factor = 0.8

It shows that except for the case where the estimated refrigerant power is 9500 W, the model and the tests match within 5% for a correction factor $\beta_h = 0.8$. It is not clear why our model underestimates the refrigerant power for high volumetric flow rates. One possible explanation is that the volumetric flow rate was measured when the refrigerant was not in fully liquid state. In this case, the mass flow rate would be overestimated and therefore the measured refrigerant power would be overestimated as well.

3.3 Comparison of Ford Escape Models

These models were developed and tuned for one specific vehicle. They are all based on Artificial Neural networks ANNs trained on data generated from the vehicle tests. The comparisons show plots of predicted vs. training data, including experimental scatter.

3.3.1 Direct ANN Engine model— was trained to directly correlate the engine coolant temperature to the engine state given by: vehicle speed (m/s), load (N), coolant volumetric flow rate (lpm) and inlet coolant temperature (^oC).

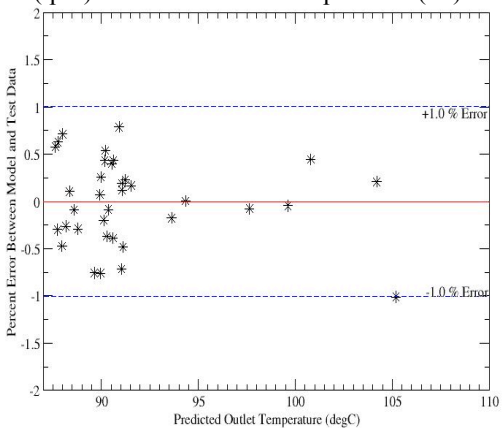

Figure 23: ANN-Engine model prediction of outlet temperature (^oC)

The ANN was specified in static configuration with a 4-5-1 topology (4 inputs, 5 neurons in one hidden layer and 1 output). The model was trained such that the normalized cumulative prediction error decreased by 2 orders of magnitude.

Model-test data comparisons are shown in Figure 23. The figures show that the ANN model predictions are well within the desired 5% of test data (within 1% in this case).

3.3.2 Coolant Pump Models— relate the coolant mass flow rates in the engine and transaxle cooling loops to the vehicle speed (m/s) and load (N). Both static ANNs were specified with a 2-5-5-1 topology (2 inputs, 5 neurons in first hidden layer, 5 neurons in second and 1 output). The results are shown in Figures 24 and 25, and show that all ANN model predictions are within the desired 5% of test data.

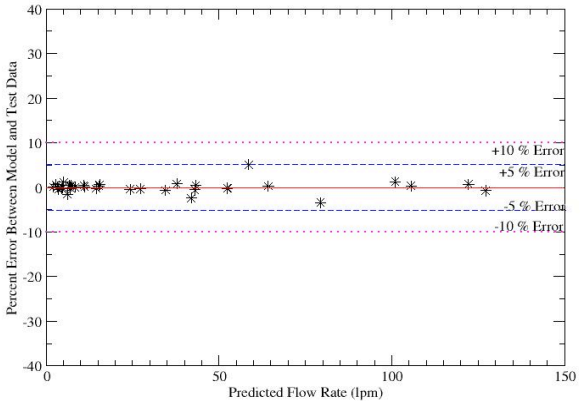

Figure 24: ANN-Pump model prediction of engine coolant flow rate (lpm)

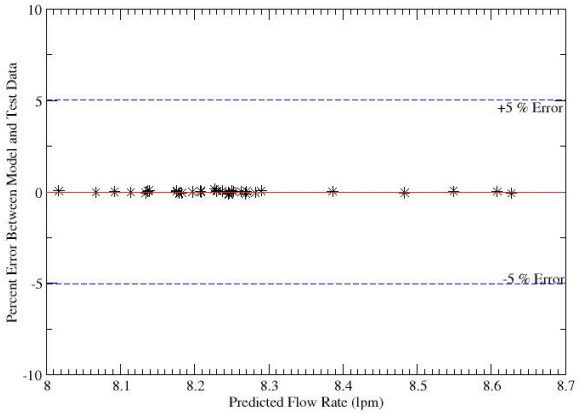

Figure 25: ANN-Pump model prediction of transaxle coolant flow rate (lpm)

3.3.3 Transaxle Heating Model— relates the coolant temperature at the inlet to the transaxle radiator (transaxle outlet) to the to the vehicle speed (m/s), load (N), coolant

volumetric flow rate (lpm) and inlet temperature (^{o}C). The ANN was specified in a static configuration and had a 4-5-1 topology (4 inputs, 5 neurons in one hidden layer and 1 output). The model was trained such that the cumulative prediction error decreased by 3 orders of magnitude.

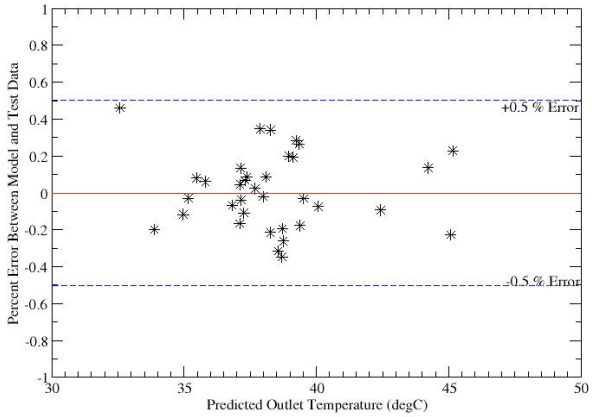

Figure 26: ANN-M/E Unit model prediction of outlet temperature (^{o}C)

Model-test data comparisons are shown in Figure 26. The figures show that the ANN model predictions are well within the desired 5% of test data (within 0.5% in this case).

4. SUMMARY AND CONCLUSIONS

Simulation-based prototyping of complex systems can be very challenging in terms of domain grid complexity, density and the associated long simulation times. A practical alternative is to partition such systems into interacting component models of desired resolution and fidelity and couple the execution of these models into an integrated computational scheme. The resultant multi-resolution co-simulations can provide an optimum balance between desired accuracy, simulation times, and computational resources. Moreover, interchanging component models of different resolution allows one to selectively focus-in on the details of their operation, in the context of whole-system dynamics. This approach is of particular importance in the virtual, simulation-based prototyping of thermal management strategies for complex cooling systems embedded in vehicle under-the-hood systems for which the use of full CFD analysis is impractical.

The first two examples showed the accuracy, speed and the stability of the multi-resolution approach. In general, the acceleration of execution times compared to full CFD analysis is due to lower number of computational cells resulting from replacement of fully gridded system components by equivalent reduced models. Execution of even complex reduced models such as those associated with the A/C system can be timed in terms of milliseconds; in comparison to their gridded equivalents, the computational time spent in execution of such models is therefore essentially insignificant. For modern vehicles with multiple heat generating components, the multi-resolution approach can thus be the enabling methodology for performing system-level thermal management prototyping simulations.

ACKNOWLEDGEMENTS

This research was performed under the Army TACOM SBIR Phase II Project "Co-Simulation Software For Rapid Prototyping Of Vehicle Cooling Systems", Contract Number W56HZV-09-C-0056.

REFERENCES

Astina, I. Made and Sato, H*, (2004), "Fundamental equation of state for 1,1,1,2-tetrafluoroethane with an intermolecular potential energy background and reliable ideal-gas properties",* Fluid Phase Equilibria 221 (2004).

Gnielinski, V., (1976), "New equations for heat and mass transfer in turbulent pipe and channel flow", Int. Chem Engineering, **16**, pp. 359-368.

Jung D., and Assanis D.N. (2006), "Numerical Modeling of Cross Flow Compact Heat Exchanger with Louvered Fins using Thermal Resistance Concept", SAE Technical Paper 2006-01-0726.

Pindera,, M.Z., Sun, Y., Malosse, J-J, and Vosen, S.R., (2014), "Multi-Resolution Rapid Prototyping of Vehicle Cooling Systems", Proceedings of the 2014 IEEE

Krauss, R., Luettmer-Strathmann, J., Sengers, J.V., and Stephan, K., (1993), "*Transport Properties of 1,1,1,2-Tetrafluoroethane (R 134a)*", Int. J. of Thermophysics, **14**:4.

Pindera, M.Z. (2009), "Multiresolution Thermal Design/Signature Management Tools For Vehicle Electronics Packages," Phase II Final Report; Army Contract Number: W56HZV-06-C-0571.

Rasmussen B.P. (2002), "*Control oriented modeling of transcritical vapor compression systems",* M.S Thesis, University of Illinois at Urbana-Champaign, 2002.

Shah, R. (2003), "*Dynamic Modeling and Control of Single and Multi-Evaporator Subcritical Vapor Compression Systems*", M.S. Thesis, University of Illinois at Urbana-Champaign.

Siegel, J., 2007, Corba 3 *Fundamentals and Programming*, John Wiley & Sons, University of Michigan.

Yata, J., Ueda, Y., and Horis, M., (2005), "*Equations for the Thermal Conductivity of R-32, R-125, R-134a, and R-143a*", Int. J. of Thermophysics, **26**:5, Sept.